Available online at www.synsint.com

Synthesis and Sintering

ISSN 2564-0186 (Print), **ISSN** 2564-0194 (Online)

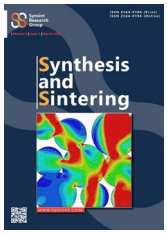

Research article

Morphology-driven mechanical behavior of sintered titanium: A meso-scale numerical study

Ata Khabaz-Aghdam [a,*], **Bahati M. Clément** [a], **Abuzar E'shagi-Oskui** [b,c]

[a] *Department of Aeronautical Engineering, Faculty of Aviation and Space Sciences, University of Kyrenia, Kyrenia, Mersin 10, Turkey*
[b] *Moganshan Institute ZJUT, Kangqian District, Deqing 313200, China*
[c] *High-speed Rotating Machinery Laboratory, College of Energy Engineering, Zhejiang University, Hangzhou 310027, China*

A B S T R A C T

The mechanical behavior of sintered microstructures is strongly influenced by their underlying morphology, particularly particle arrangement, size distribution, and inter-particle connectivity. In this study, a meso-scale numerical framework was developed to investigate the structure–property relationships of sintered titanium microstructures using randomly generated two-dimensional models. Nine representative configurations with varying overlap levels (5, 10, and 15 µm) were analyzed under directional loading conditions, resulting in a total of eighteen simulations. The results demonstrate, within the adopted two-dimensional meso-scale framework, that increasing particle overlap significantly enhances neck formation, leading to improved load transfer, higher stiffness, and increased strength. Specifically, the Young's modulus increased from as low as 0.3 GPa in low-overlap cases to values exceeding 60 GPa in highly connected structures, while the ultimate strength reached up to 415 MPa. The coefficient of variation (CV), ranging from 0.15 to 0.30, was found to strongly influence mechanical performance, with higher values promoting heterogeneity, stress concentration, and strain localization. In contrast, increased connectivity (Z_{av} = 2.00–2.73) improved load distribution and mechanical stability by providing multiple load paths. To capture the combined effects of microstructural heterogeneity, a randomness index (RI = 0.07–0.14) was introduced as a unified descriptor. The RI showed a strong inverse correlation with both stiffness and strength, outperforming individual parameters such as CV and connectivity. Furthermore, the mechanical response was found to be highly anisotropic, with stiffness ratios (E_y/E_x) varying from 0.01 to 4.22 depending on microstructural topology and loading direction. Overall, the findings highlight the critical role of morphology in governing the mechanical performance of sintered microstructures and provide a systematic framework for the design of materials with tailored properties.

© 2026 The Authors. Published by Synsint Research Group.

KEYWORDS

Sintering
Meso-scale modeling
Morphology
Mechanical behavior
Finite element method

OPEN ACCESS

1. Introduction

Sintered materials have attracted significant attention in recent years due to their wide range of applications in aerospace, biomedical, and structural engineering. Among these materials, sintered titanium stands out because of its excellent strength-to-weight ratio, corrosion resistance, and biocompatibility. These properties make it a promising candidate for advanced engineering components where both mechanical performance and structural efficiency are critical [1–3].

* Corresponding author. *E-mail address:* ata.khabazaghdam@kyrenia.edu.tr (A. Khabaz-Aghdam)
Received 27 February 2026; Received in revised form 24 March 2026; Accepted 30 March 2026.
Peer review under responsibility of Synsint Research Group. This is an open access article under the CC BY license (https://creativecommons.org/licenses/by/4.0/).
https://doi.org/10.53063/synsint.2026.61332

Their microstructure inherently governs the mechanical behavior of sintered materials. Unlike fully dense materials, sintered microstructures consist of discrete particles connected through inter-particle necks, resulting in a highly heterogeneous and porous structure. This complex morphology plays a crucial role in determining load transfer mechanisms, deformation patterns, and failure behavior. In particular, parameters such as particle size distribution, degree of connectivity, and neck formation significantly influence stiffness, strength, and strain localization [4–6].

Previous studies have investigated the relationship between microstructure and mechanical properties using both experimental and numerical approaches [7–9]. Experimental techniques, such as scanning electron microscopy (SEM) and mechanical testing, have provided valuable insights into the evolution of microstructure during sintering and its impact on mechanical performance [10–12]. However, experimental approaches are often limited in their ability to isolate individual morphological parameters and to study their combined effects systematically.

To overcome these limitations, numerical modeling at the meso-scale has emerged as a powerful tool for investigating structure–property relationships in sintered materials. Several studies have employed idealized or reconstructed microstructures to analyze stress distribution and deformation behavior [13–15]. Nevertheless, many existing models rely on simplified assumptions, such as uniform particle sizes or regular arrangements, which do not adequately capture the inherent randomness and heterogeneity of real sintered systems.

In recent years, efforts have been made to incorporate stochastic features into microstructural modeling. Randomly generated particle assemblies have been used to better represent realistic morphologies; however, a comprehensive framework that simultaneously considers particle size variability, inter-particle connectivity, and neck formation is still lacking. Moreover, the combined influence of these parameters on anisotropic mechanical behavior remains insufficiently understood [16–18].

In this context, the present study aims to develop a systematic meso-scale numerical framework to investigate the morphology-driven mechanical behavior of sintered titanium microstructures. Random two-dimensional microstructures are generated using a custom MATLAB-based algorithm, allowing controlled variation of particle overlap, size distribution, and connectivity. A set of nine representative configurations is analyzed under directional loading conditions to evaluate the influence of morphological parameters on stress distribution, strain localization, stiffness, and strength. The proposed framework is intended to provide insight into the relative influence of microstructural morphology on mechanical response and to establish structure-property relationships, rather than to reproduce the exact behavior of a specific experimentally manufactured sintered titanium material.

A key contribution of this work is the introduction of a randomness index (RI) as a unified descriptor of microstructural heterogeneity. This parameter integrates the effects of particle size dispersion and connectivity, providing a more comprehensive measure of structural disorder compared to conventional descriptors. The correlation between *RI* and mechanical response is systematically investigated and compared with individual morphological parameters.

The results of this study provide new insights into the fundamental mechanisms governing load transfer and deformation in sintered microstructures. While the developed numerical framework is primarily intended for mechanistic and comparative analysis, the predicted mechanical responses are discussed in the context of experimentally reported ranges for porous and sintered titanium materials available in the literature. By establishing clear structure–property relationships, this work contributes to the development of microstructure-informed design strategies for sintered materials with tailored mechanical performance.

2. Materials and methods

2.1. Microstructure generation

In this study, two-dimensional synthetic microstructures representing sintered titanium were generated using a custom-developed MATLAB script. The microstructure was modeled as an assembly of circular particles with randomly assigned radii, enabling the representation of the inherent heterogeneity of powder-based materials.

To minimize boundary-induced artifacts, the particle assembly was initially constructed within an extended square domain of 500 × 500 μm^2. Particle radii were randomly selected from a uniform distribution in the range of 50–100 μm, consistent with typical powder size variations in sintering processes. After generation, a central region of 400 × 400 μm^2 was extracted by removing a 50 μm margin from each boundary. This cropping step reduces boundary effects such as truncated particles and artificial geometric constraints. Nine different configurations of sintered titanium are shown in Fig. 1. A sequential growth algorithm was employed to generate a fully connected microstructure. The first particle was placed near the center of the domain, and subsequent particles were added iteratively. At each step, a new particle was positioned relative to an existing one such that geometric connectivity was ensured while avoiding excessive overlap. This procedure resulted in a single continuous cluster without isolated particles.

2.1.1. Overlap-based representation of sintering

Inter-particle bonding was modeled through a controlled overlap approach to approximate the formation of sintering necks. Three overlap levels were considered: 5 μm, 10 μm, and 15 μm. For each pair of interacting particles, the center-to-center distance was defined as in Eq. 1.

$$d_{ij} = r_i + r_j - \delta \tag{1}$$

where r_i and r_j are the radii of the particles, and δ is the prescribed overlap. This formulation ensures contact between particles while limiting unrealistic interpenetration. An additional constraint was imposed to prevent overlap beyond the prescribed value, thereby maintaining physical consistency and ensuring that the overlap represents a simplified approximation of neck formation rather than material intermixing.

2.1.2. Porosity evaluation and domain cropping

A target porosity of 40% was imposed for all generated microstructures (within an extended square domain of 500 × 500 μm^2). However, the porosity was recomputed after cropping (for the 400 × 400 μm^2 domain models shown in Fig. 1), and all reported values correspond to the final domain used for analysis. This procedure improves the statistical representativeness of the microstructure. The computational domain was discretized into a uniform grid, and each grid point was classified

as solid if it fell within any particle. The solid fraction was then determined, and porosity was calculated as Eq. 2.

$$\varphi = 1 - \frac{A_{solid}}{A_{total}} \quad (2)$$

The generation process continued iteratively until the target porosity was achieved. This approach inherently accounts for particle overlap and avoids overestimation of the solid fraction.

2.1.3. Parametric design

A total of nine independent microstructures were generated to investigate the influence of inter-particle overlap. The parametric design consisted of three overlap levels (5, 10, and 15 μm), with three independent random realizations for each level. For each microstructure, the particle center coordinates, particle radii, prescribed overlap, and final porosity were recorded. These datasets were subsequently used for morphological analysis and numerical simulations.

For each overlap level (5, 10, and 15 μm), three statistically independent microstructures were generated using different random seeds in the MATLAB algorithm. While the target porosity, particle size range (50–100 μm), and overlap level were kept constant within each group, the particle center coordinates and the resulting particle arrangements were

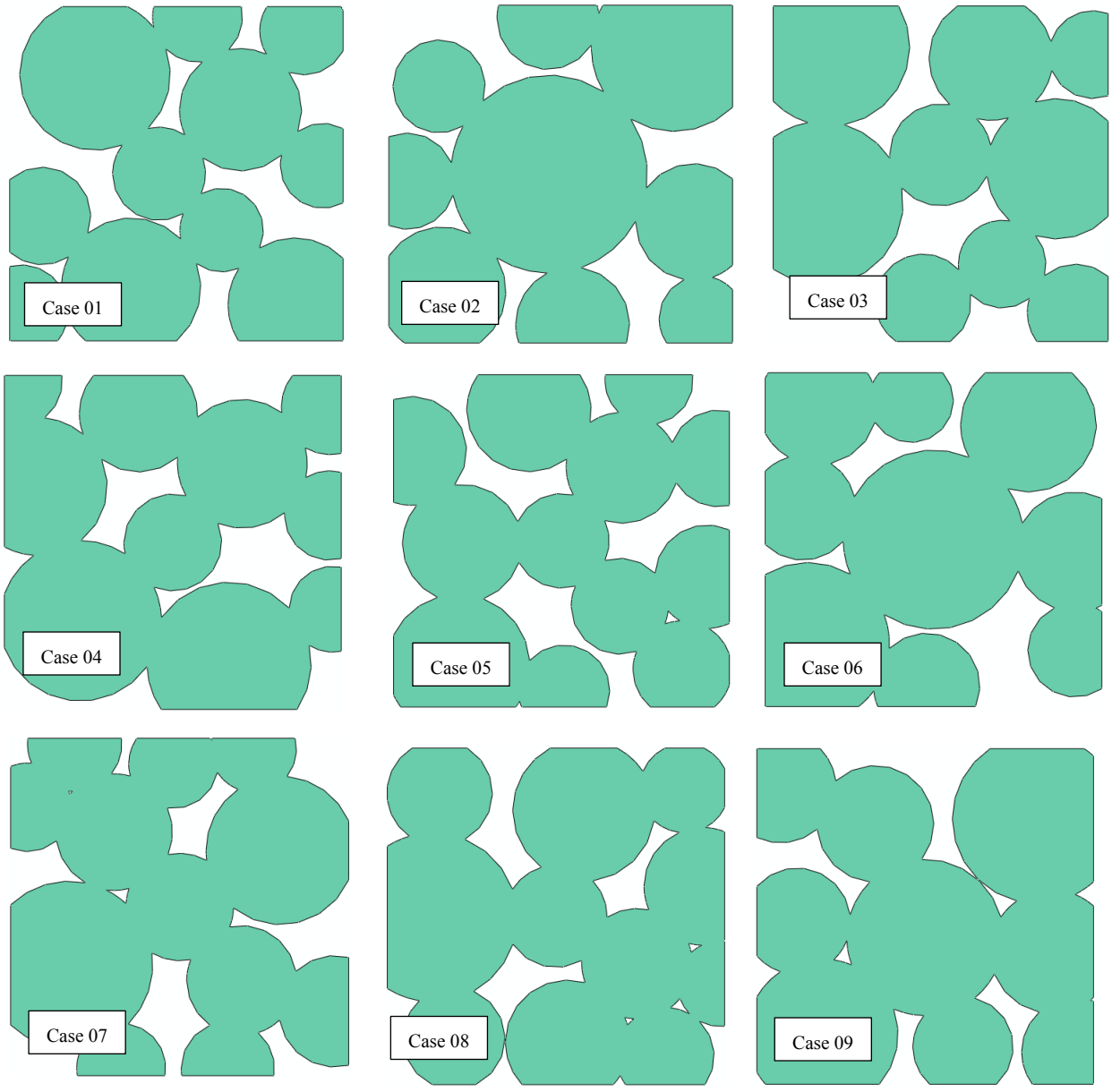

Fig. 1. Generated microstructures of sintered titanium. Cases 01–03, cases 04–06, and cases 07–09 correspond to three independent random realizations generated with overlap lengths of 5, 10, and 15 μm, respectively. Within each group, the overlap level, particle-size range, and target porosity were maintained, while particle locations and resulting microstructural topology were generated independently using different random seeds.

randomly generated for each realization. Consequently, cases 01–03, cases 04–06, and cases 07–09 represent independent stochastic realizations of the same overlap condition, differing in particle spatial distribution, local connectivity, coordination number, anisotropy, and particle-size statistics. This approach enables the influence of overlap to be evaluated while simultaneously accounting for the inherent variability associated with random microstructural morphology.

2.2. Morphological characterization

To establish a quantitative relationship between microstructure and mechanical response, several morphology descriptors were defined and computed for each configuration, including particle size distribution, degree of connectivity, neck ratio, geometrical anisotropy, and a randomness index.

2.2.1. Particle size distribution

The coefficient of variation (CV) was used as a dimensionless parameter to quantify the dispersion of particle sizes within the generated microstructures. It is defined as the ratio of the standard deviation of particle radii to their mean value.

$$\bar{r} = \frac{1}{n}\sum_{i=1}^{n} r_i \tag{3}$$

$$\sigma_r = \sqrt{\frac{1}{n}\sum_{i=1}^{n}(r_i - \bar{r})^2} \tag{4}$$

$$CV = \frac{\sigma_r}{\bar{r}} \tag{5}$$

where σ_r is the standard deviation and $\bar{r}$ is the mean particle radius. The CV provides a normalized measure of particle size heterogeneity, allowing for direct comparison between different microstructures regardless of their absolute size scale. From a physical standpoint, lower values of CV indicate a more uniform particle size distribution, which typically leads to more homogeneous load transfer and a more stable mechanical response. In contrast, higher CV values reflect increased variability in particle sizes, resulting in more complex load paths, enhanced stress concentrations, and a higher tendency for strain localization. In the present study, the CV is further utilized as a key component of the randomness index, enabling a combined assessment of size dispersion and structural connectivity in governing the mechanical behavior of sintered microstructures.

2.2.2. Degree of connectivity

The degree of connectivity, also referred to as the coordination number, was used to quantify the average number of contacts per particle within the microstructure. This parameter reflects the level of inter-particle interaction and plays a critical role in load transfer mechanisms. Two particles were considered to be connected if the distance between their centers satisfied the following condition.

$$d_{ij} \le (r_i + r_j)\alpha \tag{6}$$

where d_{ij} is the Euclidean distance between particles i and j, r_i and r_j are their respective radii, and α is a tolerance factor introduced to account for numerical discretization, taken as 1.05 in this study. For each particle, the coordination number Z_i was calculated as the number of neighboring particles satisfying the above condition. The average degree of connectivity for the entire microstructure was then obtained as Eq. 7.

$$Z_{av} = \frac{1}{n}\sum_{i=1}^{n} Z_i \tag{7}$$

where n is the total number of particles. Physically, higher values of Z_{av} indicate a more interconnected microstructure with multiple load transfer paths, which generally enhances mechanical stiffness and strength. Conversely, lower values of Z_{av} correspond to sparsely connected structures, leading to stress concentration and an increased likelihood of localized deformation and failure. In the present work, Z_{av} is also employed in combination with the coefficient of variation to define the randomness index, providing a unified descriptor of microstructural heterogeneity.

2.2.3. Neck ratio (δ/r)

The neck ratio was introduced as a measure of the effective bonding between adjacent particles within the microstructure. In sintered materials, inter-particle necks play a crucial role in governing load transfer and mechanical strength. Since the exact neck geometry was not explicitly modeled, an approximate definition based on particle overlap was adopted. For two interacting particles, the overlap parameter δ_{ij} was defined as Eq. 8, where r_i and r_j are the particle radii and d_{ij} is the distance between their centers. For overlapping particles ($\delta_{ij}>0$), the neck ratio was defined as Eq. 9.

$$\delta_{ij} = r_i + r_j - d_{ij} \tag{8}$$

$$\text{Neck ratio} = \frac{\delta}{r} = \frac{\delta_{ij}}{\min(r_i, r_j)} \tag{9}$$

This normalization ensures that the neck size is evaluated relative to the smaller particle, providing a consistent measure of inter-particle bonding. The average neck ratio over all interacting particle pairs was used as a representative parameter for each microstructure. From a physical perspective, higher neck ratio values indicate stronger inter-particle bonding and improved load transfer efficiency, which generally enhances stiffness and strength. In contrast, lower neck ratios correspond to weaker connections, leading to reduced load-bearing capacity and increased susceptibility to localized deformation.

2.2.4. Geometrical anisotropy

To quantify the directional dependency of the microstructure, a geometrical anisotropy index was defined based on the spatial distribution of particle centers. The second-order spatial moments of particle positions were calculated as in Eq. 10. The anisotropy index was then defined as in Eq. 11.

$$I_x = \sum_{i=1}^{n} y_i^2, \quad I_y = \sum_{i=1}^{n} x_i^2 \tag{10}$$

$$AI = \frac{\max(I_x, I_y)}{\min(I_x, I_y)} \tag{11}$$

A value of AI≈1 indicates an approximately isotropic structure, whereas deviations from unity reflect anisotropic particle distributions. Physically, geometrical anisotropy can lead to direction-dependent mechanical behavior, where stiffness, strength, and deformation patterns differ along different loading directions. This is particularly relevant in the present study, where each microstructure is subjected to both horizontal and vertical loading conditions.

2.2.5. Randomness index (RI)

To provide a unified measure of microstructural heterogeneity, a randomness index (RI) was defined by combining the effects of particle size dispersion and connectivity.

$$RI = \frac{CV}{Z_{av}} \quad (12)$$

Where CV is the coefficient of variation of particle radii and Z_{av} is the average coordination number. This index increases with increasing size variability and decreasing connectivity, representing a higher degree of structural disorder. Conversely, lower values of RI correspond to more uniform and well-connected microstructures. The proposed randomness index serves as a key parameter in this study, enabling direct correlation between microstructural characteristics and mechanical response, particularly in terms of stress distribution and strain localization.

2.3. Numerical simulation framework

The mechanical response of the generated sintered titanium microstructures was investigated using two-dimensional finite element analysis (FEA) at the meso-scale. Although real sintered titanium microstructures are inherently three-dimensional, a two-dimensional representation was adopted in this study to enable a systematic investigation of morphology–property relationships while maintaining computational efficiency. The primary objective of the work is not to predict the absolute mechanical properties of a specific sintered component, but rather to identify the relative influence of morphological descriptors such as particle size variability, connectivity, neck ratio, and randomness index on the mechanical response. Similar two-dimensional meso-scale approaches have been widely employed in the literature to investigate load-transfer mechanisms, stress localization, and microstructure-induced anisotropy in particulate and porous materials. The adopted framework therefore provides a computationally efficient platform for isolating the effects of microstructural morphology and establishing qualitative structure–property trends.

The geometries created in MATLAB were imported into the finite element environment and discretized using a structured mesh. All simulations were performed under plane stress conditions using 4-node bilinear quadrilateral elements with reduced integration and hourglass control (CPS4R). A uniform mesh size of 3 μm was employed for all models. This mesh density was selected based on a mesh convergence study to ensure the accuracy and stability of the numerical results, particularly in regions with high stress gradients such as inter-particle necks. A representative mesh configuration for case 01 is shown in Fig. 2.

The material used in this study was titanium, modeled as an isotropic elastic–perfectly plastic material. The elastic properties were defined by a Young's modulus of 114 GPa and a Poisson's ratio of 0.3. Plastic behavior was incorporated using a von Mises yield criterion with a yield strength of 1170 MPa, assuming no strain hardening.

All microstructures had identical overall dimensions of 400 × 400 μm^2. The mechanical response was evaluated under displacement-controlled loading conditions in two orthogonal directions: horizontal (X-direction) and vertical (Y-direction).

For loading in the X-direction, the left boundary of the model was constrained in the horizontal direction (U_x = 0), while the bottom boundary was constrained in the vertical direction (U_y = 0) to prevent rigid body motion. The right boundary was coupled to a reference point, and a uniform displacement of 15 μm was applied in the X-direction. For loading in the Y-direction, an analogous boundary condition was applied by constraining the bottom boundary in the vertical direction and applying a vertical displacement of 15 μm to the top boundary through a coupled reference point, while restricting horizontal rigid body motion. Schematic illustrations of the applied boundary conditions for both X and Y loading directions is presented in Fig. 3 for case 01. The simulations were carried out under quasi-static conditions, and the nonlinear response due to plastic deformation was captured using an implicit solution scheme. Since inter-particle bonding was predefined through geometric overlap, all particles were considered to be perfectly bonded, and no additional contact formulation was required. In total, 18 simulations were performed, corresponding to nine microstructures subjected to two orthogonal loading directions. The numerical results were subsequently correlated with the morphological parameters defined in Section 2.2 to establish structure–property relationships.

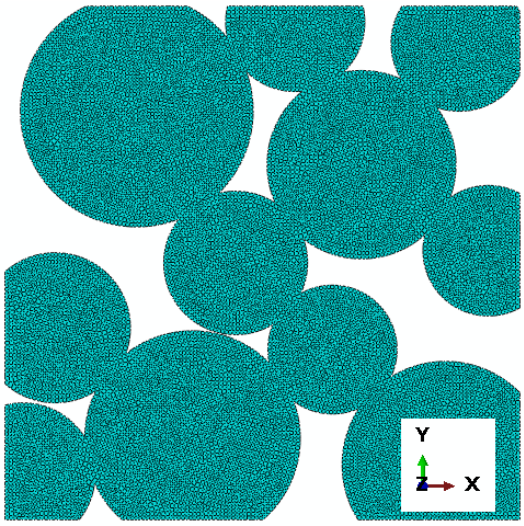

Fig. 2. Finite element mesh of the generated microstructure (case 01) using CPS4R elements with a uniform element size of 3 μm.

3. Results and discussion

3.1. Morphological analysis

The calculated morphological parameters for the nine generated microstructures are summarized in Table 1. The models were categorized into three groups based on the prescribed overlap length (5 μm, 10 μm, and 15 μm), allowing for a systematic investigation of the influence of inter-particle bonding on the structural characteristics.

3.1.1. Overlap on neck formation

As expected, the average neck ratio increases significantly with increasing overlap length. For the cases with 5 μm overlap (case 01–case 03), the neck ratio ranges from 0.078 to 0.09. Increasing the overlap to 10 μm (case 04–case 06) results in a substantial rise in neck ratio to approximately 0.15–0.16. A further increase to 15 μm (case 07–case 09) leads to even larger values, reaching up to 0.23. This trend

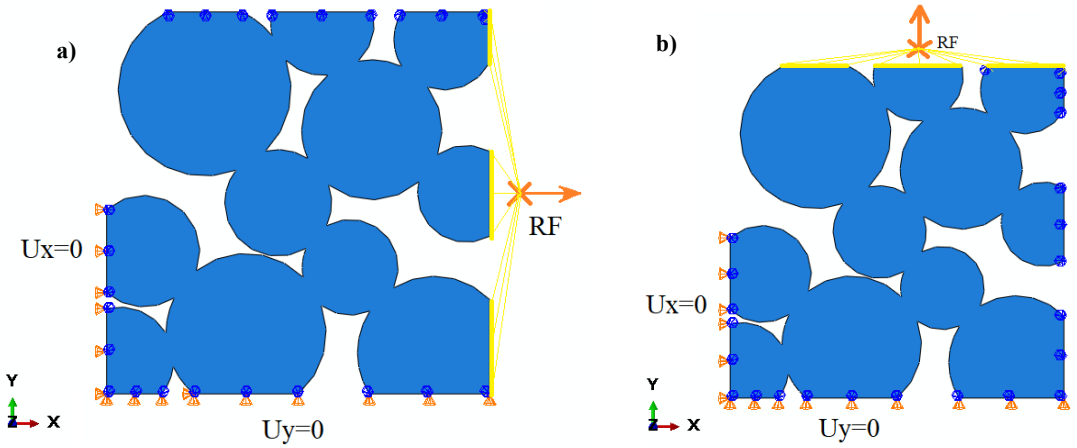

Fig. 3. Applied boundary conditions for a) X-direction loading and b) Y-direction loading for case 01. Displacement-controlled loading is applied through a reference point, while appropriate constraints are imposed to prevent rigid body motion.

confirms that the overlap parameter effectively controls the extent of inter-particle bonding, directly influencing the mechanical load transfer capability of the microstructure. Stronger neck formation at higher overlap levels is expected to enhance stiffness and reduce stress concentration.

3.1.2. Particle size distribution and variability

The mean particle radius across all models varies between approximately 63 µm and 76 µm, indicating a relatively consistent size scale among the generated microstructures. However, the standard deviation and coefficient of variation (CV) exhibit noticeable differences between cases.

The CV ranges from 0.1482 (case 05) to 0.3045 (case 02), reflecting varying degrees of particle size heterogeneity. Notably, case 02 exhibits the highest CV, indicating a highly non-uniform particle distribution, while case 05 shows the most uniform structure. From a mechanical perspective, higher CV values are associated with increased heterogeneity, which can lead to irregular load paths and localized stress concentrations. In contrast, lower CV values correspond to more uniform stress distribution and potentially more stable mechanical behavior.

3.1.3. Connectivity and load transfer

The average degree of connectivity (Z_{av}) varies between 2.00 and 2.73 across all cases. The lowest connectivity is observed in case 05, while the highest value appears in case 08. Although the overlap length increases from 5 µm to 15 µm, the coordination number does not exhibit a strictly monotonic trend. This indicates that connectivity is not solely governed by overlap, but is also strongly influenced by the random spatial arrangement and particle size distribution. Higher values of Z_{av} suggest the presence of multiple load transfer paths, which can improve structural integrity and delay the onset of localized deformation.

3.1.4. Geometrical anisotropy

The anisotropy index (AI) varies between 1.02 and 1.43, indicating that all generated microstructures are close to isotropic but still exhibit measurable directional variations. The highest anisotropy is observed in case 03 and case 08, suggesting a more directionally biased particle distribution. Such anisotropy can result in direction-dependent mechanical responses, which is particularly relevant given that each model is subjected to loading in both horizontal and vertical directions.

Table 1. Summary of the morphological characteristics of the generated microstructures, including particle size distribution, neck formation, connectivity, geometrical anisotropy, and randomness descriptors.

	Overlap length (d_{ij}), µm	Average neck ratio (δ/r)	Mean radius ($\bar{r}$), µm	Standard deviation of radius (σ_r), µm	Coefficient of variation (CV= $\sigma_r/\bar{r}$)	Anisotropy index (AI=I_x/I_y)	Randomness index (RI=CV/Z_{av})	Average degree of connectivity (Z_{av})
Case 01	5	0.09	64.18	14.80	0.23	1.21	0.10	2.36
Case 02	5	0.08	72.53	22.09	0.30	1.16	0.14	2.22
Case 03	5	0.08	70.08	17.95	0.26	1.43	0.12	2.22
Case 04	10	0.15	70.16	17.39	0.25	1.04	0.11	2.20
Case 05	10	0.16	63.68	9.44	0.15	1.13	0.07	2.00
Case 06	10	0.15	73.29	18.74	0.26	1.07	0.12	2.22
Case 07	15	0.23	64.29	15.20	0.24	1.24	0.10	2.33
Case 08	15	0.20	67.28	14.50	0.22	1.39	0.08	2.73
Case 09	15	0.20	75.57	15.04	0.2	1.02	0.09	2.22

3.1.5. Randomness index and structural disorder

The randomness index (RI), defined as a combination of particle size variability and connectivity, ranges from 0.07 to 0.14. The highest RI value is observed in case 02, which corresponds to the highest CV and relatively low connectivity. Conversely, case 05 exhibits the lowest RI, indicating a more ordered and uniform structure. This parameter provides a comprehensive measure of microstructural disorder. Higher RI values are associated with increased heterogeneity and reduced connectivity, which are expected to promote strain localization and non-uniform deformation patterns.

3.2. Mechanical response

3.2.1. Stress distribution and load transfer mechanisms

The von Mises stress distributions for all nine microstructures under X and Y-directional loading are presented in Fig. 4. The red regions indicate regions of high stress concentration and the onset of plastic deformation, providing critical insight into load transfer mechanisms and deformation patterns.

Across all cases, stress localization is consistently observed at inter-particle contact regions, confirming that necks serve as the primary load-bearing elements within the microstructure. However, the distribution, intensity, and continuity of these high-stress regions vary significantly depending on overlap level and microstructural morphology. In particular, these regions correspond to critical regions where load transfer occurs through limited pathways, making them highly susceptible to plastic initiation.

In all microstructures, stress is predominantly concentrated at particle contacts. This indicates that load transfer occurs through discrete neck regions rather than uniformly across particles. As a result, the mechanical response is governed by the topology of the contact network. Moreover, the orientation and spatial distribution of these contacts determine whether the load is transmitted through multiple distributed paths or through a limited number of dominant load chains.

A clear transition in stress patterns is observed with increasing overlap. In cases 01–03 with low overlap, stress is highly localized at a limited number of contacts. Load transfer is discontinuous, and deformation is governed by a few critical paths, leading to pronounced stress

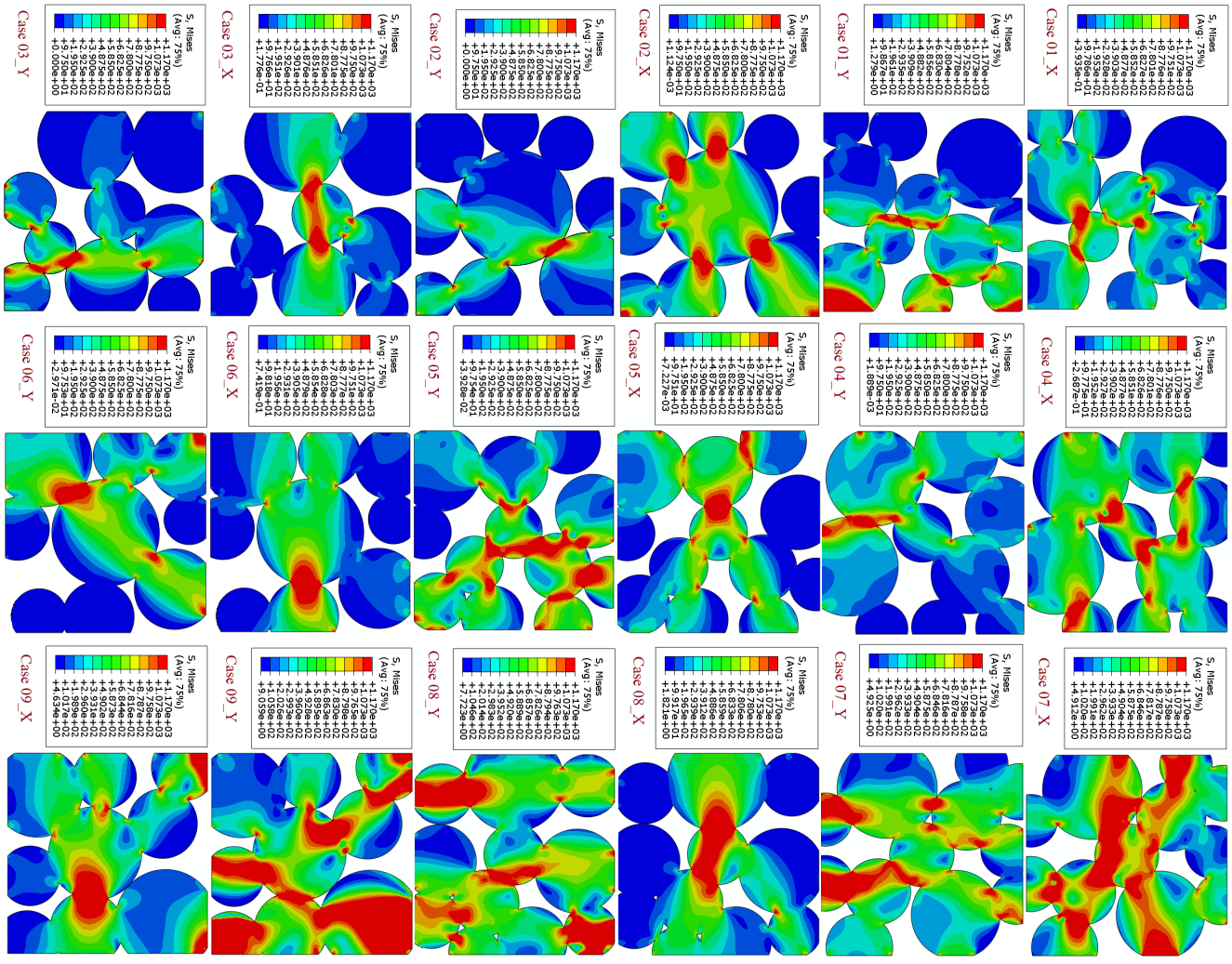

Fig. 4. Von Mises stress contours of the microstructures under X and Y loading.

concentration. An extreme example of this behavior is observed in case 02 under Y-direction loading. Although the microstructure remains geometrically connected, the specific particle arrangement restricts load transfer to a narrow load-bearing path. Consequently, deformation becomes highly localized, resulting in a markedly reduced effective stiffness. This behavior highlights the strong influence of local topology on the mechanical response of finite-sized random microstructures and demonstrates that individual realizations may exhibit responses that differ substantially from the homogenized behavior of bulk sintered materials.

For cases 04–06 within moderate overlap, stress distribution becomes more spread, with multiple active load paths. Localization still exists but is less intense compared to low-overlap cases. For cases 07–09 with high overlap, stress fields become more continuous, forming broader load transfer regions. This indicates improved load-sharing capability, enhanced structural integrity, and reduced sensitivity to local defects.

For all cases, significant differences are observed between X and Y loading directions. In many Y-loaded cases (e.g., case 01_Y, case 05_Y, case 08_Y), a continuous vertical stress band is formed, indicating the development of a dominant load path aligned with the loading direction. In contrast, X-loading cases generally exhibit more distributed and multi-directional stress paths, suggesting a more diffuse load transfer mechanism. This indicates that even randomly generated microstructures exhibit emergent anisotropy, governed by particle arrangement and connectivity. Furthermore, the observed stress patterns suggest that anisotropy is not only geometrical but also mechanical, as the preferred load paths lead to direction-dependent stiffness and deformation behavior. In addition, two distinct stress localization mechanisms can be identified across the microstructures. In relatively aligned particle arrangements, stress localization is dominated by normal stresses, forming continuous bands along the loading direction. In contrast, more irregular and heterogeneous structures exhibit shear-dominated localization, characterized by isolated and highly concentrated stress regions at particle contacts. These differences play a critical role in governing the onset of plastic deformation and subsequent failure behavior.

3.2.2. Strain localization and plastic deformation patterns

The equivalent strain distributions for all nine microstructures under X and Y-directional loading are presented in Fig. 5. The highlighted regions indicate zones of high strain concentration, corresponding to the initiation and progression of plastic deformation within the microstructure.

Across all cases, plastic deformation is predominantly localized at inter-particle neck regions, consistent with the stress concentration patterns observed in the von Mises distributions. These regions act as mechanically weak zones where deformation is initiated due to limited load transfer area and geometric discontinuities. A notable feature observed in all microstructures is that plastic strain tends to develop along curved and interconnected paths, rather than in a purely linear manner. These curved deformation paths follow the geometry of particle arrangements and reflect the natural load transfer pathways within the heterogeneous structure. This behavior highlights that plastic deformation is strongly governed by the topology of the contact network rather than by a uniform material response.

Furthermore, the extent and path of strain localization are highly dependent on the loading direction. In most cases, the regions of maximum strain shift significantly between X and Y loading conditions, indicating that the onset of plastic deformation is direction-sensitive. This directional dependency is particularly evident in cases where distinct deformation paths emerge along the loading direction, forming quasi-continuous strain bands.

In microstructures with lower overlap (cases 01–03), strain localization is highly concentrated within limited neck regions, leading to sharp and intense deformation zones. As the overlap increases (cases 04–06), the strain distribution becomes more diffuse, with multiple active deformation paths within the structure. For high overlap cases (cases 07–09), strain fields appear more distributed and continuous, indicating improved deformation compatibility and reduced localization intensity. Additionally, the morphology of the strain field suggests the coexistence of different deformation mechanisms. In relatively aligned particle configurations, deformation is dominated by normal strains along preferred load paths. In contrast, more irregular arrangements promote shear-dominated deformation, resulting in curved and non-linear strain localization patterns.

3.2.3. Stress–strain response of microstructures

The stress–strain responses of all nine microstructures under X and Y-directional loading are presented in Fig. 6, while the corresponding quantitative values of Young's modulus and yield strength are summarized in Table 2. For clarity, the curves are grouped into three sets according to overlap levels: cases 01–03 (low overlap), cases 04–06 (moderate overlap), and cases 07–09 (high overlap).

As observed from Fig. 6, the stress–strain curves are widely scattered, indicating a strong dependence of mechanical response on microstructural morphology. This variability is further confirmed by the values listed in Table 2, where both stiffness and strength exhibit significant differences across the cases and loading directions.

The lowest mechanical response is observed for case 02 under Y-direction loading, where the Young's modulus is only 0.3 GPa, and the yield strength is limited to 7.46 MPa. This extremely weak response is consistent with the previously observed severe stress localization, where deformation is concentrated within a narrow region, resulting in inefficient load transfer and almost negligible global stiffness. In contrast, the highest mechanical performance is observed in case 08 under Y-direction loading, where the yield strength reaches 415 MPa and the modulus increases to 63.7 GPa. Similarly, high stiffness values are observed in case 01 (E_y = 75.1 GPa) and case 04 (E_x = 52 GPa), indicating that favorable particle arrangements can significantly enhance load transfer efficiency even at lower or moderate overlap levels.

A general increasing trend in both stiffness and strength is observed with increasing overlap. In the low-overlap group (cases 01–03), the modulus and strength values are relatively low and highly scattered, reflecting limited connectivity and discontinuous load paths. In the moderate-overlap group (cases 04–06), both stiffness and strength improve, although considerable variability remains due to differences in particle arrangement. In the high-overlap group (cases 07–09), the mechanical response becomes more consistent, with relatively high stiffness (up to 43.9 GPa) and strength (up to 415 MPa), indicating enhanced inter-particle bonding and more efficient load-sharing mechanisms.

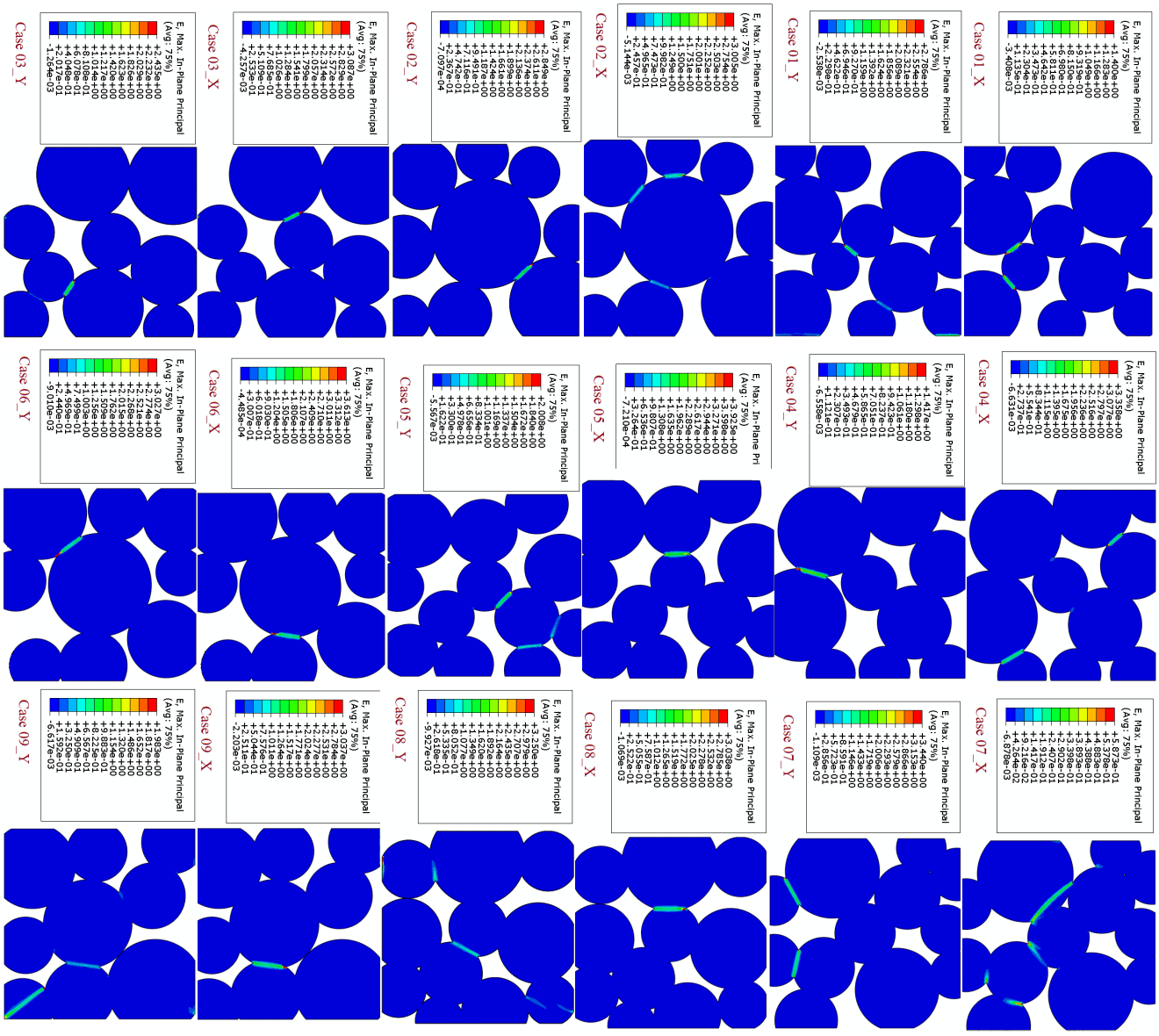

Fig. 5. Equivalent strain distributions of the nine microstructures under X and Y-directional loading. High-strain regions indicate localized plastic deformation concentrated at inter-particle necks and along curved deformation paths.

Despite this overall trend, strong directional dependency is observed in all cases. Significant differences between E_x and E_y, as well as Su_x and Su_y, indicate that the mechanical response is highly anisotropic. For example, case 01 exhibits a much higher stiffness in the Y-direction (75.1 GPa) compared to the X-direction (17.8 GPa), while case 02 shows an extreme reduction in Y-direction stiffness. Similarly, case 08 demonstrates significantly higher strength in the Y-direction (415 MPa) compared to the X-direction (231 MPa). These differences confirm that preferred load paths aligned with the loading direction play a critical role in determining mechanical performance.

Furthermore, notable variations are observed even within the same overlap group. For instance, in the moderate-overlap group, case 04 exhibits significantly higher stiffness compared to cases 05 and 06, while in the high-overlap group, case 08 outperforms cases 07 and 09 in terms of strength. These differences highlight the dominant role of microstructural topology, particularly particle arrangement and connectivity, in controlling the effective mechanical response.

3.3. Morphological influence on mechanical properties

3.3.1. Directional Young's modulus (E_x vs E_y)

The directional Young's modulus of the microstructures under X and Y loading is summarized in Table 2, along with the ratio E_y/E_x, which provides a quantitative measure of stiffness anisotropy. A value close to unity indicates an approximately isotropic response, while significant deviations reflect strong directional dependency.

The results reveal a wide range of anisotropic behavior across the microstructures. In the low-overlap group (cases 01–03), the anisotropy is particularly pronounced. Case 01 exhibits a very high ratio

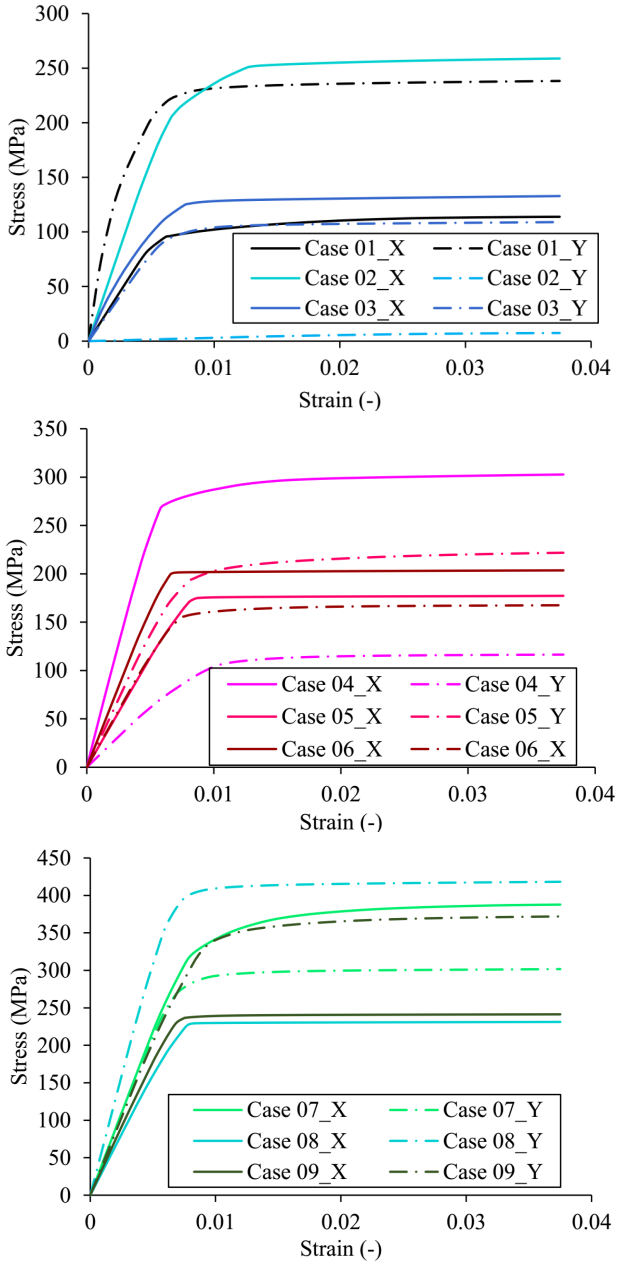

Fig. 6. Stress–strain curves of the nine microstructures under X and Y-directional loading, grouped according to overlap levels: a) cases 01–03 (low overlap), b) cases 04–06 (moderate overlap), and c) cases 07–09 (high overlap).

(E_y/E_x=4.22), indicating that the stiffness in the Y-direction is more than four times that in the X-direction. This suggests the presence of a dominant load path aligned with the Y-direction. In contrast, case 02 shows an extremely low ratio (E_y/E_x=0.01), corresponding to a nearly vanishing stiffness in the Y-direction. This behavior is consistent with severe stress localization and inefficient load transfer under Y-loading. Case 03 shows a moderate anisotropic response (E_y/E_x=0.60), indicating a partial directional dependency.

Table 2. Effective mechanical properties of the generated microstructures under X- and Y-direction loading, including Young's modulus, ultimate strength, and corresponding anisotropy ratios.

	E_x (GPa)	E_y (GPa)	E_y/E_x	Su_x (MPa)	Su_y (MPa)	Su_y/Su_x
Case 01	17.8	75.1	4.22	113	231	2.04
Case 02	33.9	0.3	0.01	257	7.5	0.03
Case 03	27.1	16.3	0.60	132	108	0.82
Case 04	52	12.6	0.24	301	116	0.39
Case 05	22.7	28.1	1.24	176	218	1.24
Case 06	33.2	23.4	0.70	203	167	0.82
Case 07	43.7	43.9	1.00	386	301	0.78
Case 08	32.5	63.7	1.96	231	415	1.80
Case 09	36.6	41.4	1.13	241	370	1.54

In the moderate-overlap group (cases 04–06), the anisotropy remains significant but becomes more balanced. Case 04 exhibits a strong directional bias toward the X-direction (E_y/E_x=0.24), while case 05 shows a slightly higher stiffness in the Y-direction (E_y/E_x=1.24). Case 06 presents a more moderate anisotropy (E_y/E_x=0.70), suggesting improved load distribution compared to the low-overlap cases.

In the high-overlap group (cases 07–09), the mechanical response becomes notably more isotropic. Case 07 exhibits an almost identical stiffness in both directions (E_y/E_x=1.00), indicating a nearly uniform load transfer network. Cases 08 and 09 show moderate anisotropy with ratios of 1.96 and 1.13, respectively, suggesting that although directional effects persist, they are less pronounced than in the low-overlap cases.

3.3.2. Directional ultimate strength (Su_x vs Su_y)

The directional ultimate strength of the microstructures under X and Y loading conditions is presented in Table 2, along with the ratio Su_y/Su_x, which quantifies the anisotropy in strength. Unlike Young's modulus, the ultimate strength is governed by the onset of failure and the maximum load-carrying capacity of the microstructure, making it highly sensitive to local deformation and failure mechanisms.

A wide variation in strength anisotropy is observed across the cases, indicating that failure behavior is strongly controlled by localized deformation patterns. In the low-overlap group (cases 01–03), the anisotropy is particularly pronounced. Case 01 exhibits a higher strength in the Y-direction (Su_y/Su_x=2.04), suggesting more efficient load transfer and delayed failure in this direction. In contrast, case 02 shows an extremely low ratio (Su_y/Su_x=0.029), indicating a severe reduction in load-carrying capacity under Y-loading. This behavior is attributed to intense strain localization within a localized region, leading to premature failure. Case 03 presents a more balanced response (Su_y/Su_x=0.82), although directional differences remain evident.

In the moderate-overlap group (cases 04–06), the ultimate strength increases overall, but anisotropy is still observed. Case 04 shows a strong directional preference toward the X-direction (Su_y/Su_x=0.39), while case 05 exhibits higher strength in the Y-direction

(Su_y/Su_x=1.24). Case 06 demonstrates a relatively moderate anisotropic behavior (Su_y/Su_x=0.82), indicating more distributed load transfer and delayed failure compared to low-overlap cases.

In the high-overlap group (cases 07–09), the ultimate strength reaches significantly higher values, and the anisotropy tends to decrease, although it does not disappear completely. Case 07 shows a relatively balanced response (Su_y/Su_x=0.78), while cases 08 and 09 exhibit higher strength in the Y-direction with ratios of 1.80 and 1.54, respectively. These results indicate that increased overlap enhances the load-bearing capacity and delays failure, while local structural features still govern the direction of failure initiation.

3.3.3. Morphology-induced anisotropy

To investigate the origin of directional mechanical behavior, the relationship between geometrical anisotropy and mechanical anisotropy is examined using the anisotropy index (AI), along with the stiffness ratio (E_y/E_x) and strength ratio (Su_y/Su_x), as summarized in Table 3.

The results indicate that all microstructures exhibit some degree of geometrical anisotropy (AI ≠ 1), although the magnitude varies across cases. However, the corresponding mechanical anisotropy, as reflected by E_y/E_x and Su_y/Su_x, shows a much wider variation, suggesting that geometrical anisotropy alone cannot fully explain the observed directional mechanical behavior. In some cases, a qualitative correlation between AI and mechanical anisotropy can be observed. For instance, case 08, which has a relatively high anisotropy index (AI = 1.39), also exhibits pronounced directional behavior, with E_y/E_x=1.96 and Su_y/Su_x=1.80, indicating enhanced stiffness and strength in the Y-direction. Similarly, case 01 shows moderate geometrical anisotropy (AI = 1.21) but a significantly higher stiffness ratio (E_y/E_x=4.22), suggesting the formation of a dominant load path aligned with the Y-direction. However, this trend is not consistent across all cases. Case 02, for example, has a comparable anisotropy index (AI = 1.16) but exhibits an extremely low stiffness and strength in the Y-direction (E_y/E_x=0.01, Su_y/Su_x=0.03). This indicates that despite a relatively moderate geometrical anisotropy, the mechanical response is governed by severe stress and strain localization, leading to inefficient load transfer and premature failure.

Table 3. Comparison between geometrical anisotropy (AI) and mechanical anisotropy measured through stiffness (E_y/E_x) and strength (Su_y/Su_x) ratios.

	AI	E_y/E_x	Su_y/Su_x
Case 01	1.213	4.22	2.04
Case 02	1.161	0.09	0.03
Case 03	1.4348	0.60	0.82
Case 04	1.0351	0.24	0.39
Case 05	1.1283	1.24	1.24
Case 06	1.0651	0.70	0.82
Case 07	1.2377	1.00	0.78
Case 08	1.3877	1.96	1.80
Case 09	1.0154	1.13	1.54

A similar discrepancy is observed in case 03 (AI = 1.44), where the mechanical anisotropy remains moderate (E_y/E_x=0.60, Su_y/Su_x=0.82), suggesting that a high geometrical anisotropy does not necessarily result in strong directional mechanical behavior. Conversely, case 07 demonstrates nearly isotropic stiffness (E_y/E_x=1.00) despite having a non-negligible geometrical anisotropy (AI = 1.2377), indicating that the load-bearing network is sufficiently well distributed to overcome geometrical irregularities.

These observations highlight that mechanical anisotropy is primarily governed by the formation and orientation of effective load paths rather than by geometrical anisotropy alone. While AI captures the global distribution of particle positions, it does not fully account for local features such as neck connectivity, particle size variation, and stress concentration, which play a critical role in determining the actual load transfer mechanism. Furthermore, the differences between stiffness anisotropy (E_y/E_x) and strength anisotropy (Su_y/Su_x) suggest that these two properties are influenced by different aspects of the microstructure. Stiffness is more sensitive to the continuity of load paths, whereas ultimate strength is strongly affected by localized deformation and failure initiation.

3.3.4. Effect of neck ratio on stiffness and strength

The influence of inter-particle neck formation on the mechanical properties is evaluated through the combined effect of overlap distance (d_{ij}) and the resulting neck ratio. The parameter d_{ij} directly controls the extent of particle overlap and therefore governs the size of the contact regions between particles, which act as the primary load transfer paths within the microstructure.

Increasing the overlap distance from 5 to 15 μm leads to a significant improvement in both stiffness and ultimate strength. This trend is further illustrated in Fig. 7, where the variation of Young's modulus (E) and ultimate strength (Su) with respect to d_{ij} is presented. Despite the inherent scatter associated with random microstructures, a clear increasing trend is observed for both mechanical properties. To quantify this relationship, exponential functions were fitted to the data. The Young's modulus follows the Eq. 13.

$$E = 7.809e^{0.1152d_{ij}}, \quad (R^2 = 0.1641) \tag{13}$$

$$Su = 53.333e^{0.1206d_{ij}}, \quad (R^2 = 0.3209) \tag{14}$$

A similar increasing trend is observed when the mechanical properties are plotted against the neck ratio (Fig. 8), confirming that the improvement in stiffness and strength is directly associated with enhanced inter-particle bonding. The correlation is more pronounced for ultimate strength, indicating that failure behavior is more sensitive to neck development than elastic response. In the low-overlap group (d_{ij} = 5 μm, cases 01–03), the mechanical response is relatively weak and highly scattered. For example, case 02 exhibits extremely low stiffness and strength in the Y-direction due to insufficient neck formation and discontinuous load paths. Under such conditions, load transfer is limited to a small number of critical contacts, resulting in severe stress localization and premature failure. With increasing overlap to 10 μm (cases 04–06), both stiffness and strength improve noticeably. The enlargement of neck regions increases the effective contact area, promoting more efficient load transfer and reducing stress concentration. However, some variability persists due to differences in particle arrangement and connectivity. In the high-overlap group

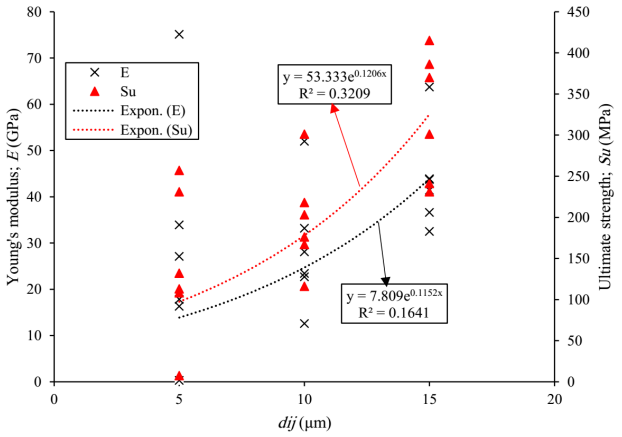

Fig. 7. Variation of Young's modulus (E) and ultimate strength (Su) as a function of overlap distance (d_{ij}). Experimental data points for all microstructures are shown along with exponential fits. Both stiffness and strength exhibit an increasing trend with increasing overlap, reflecting enhanced neck formation and improved load transfer efficiency.

(d_{ij} = 15 μm, cases 07–09), the mechanical response becomes significantly stronger and more consistent. Larger neck regions facilitate the formation of continuous load-bearing networks, allowing stresses to be distributed more uniformly across the microstructure. This results in higher stiffness values (e.g., E_x = 43.7 GPa in case 07) and increased ultimate strength (up to 415 MPa in case 08). Overall, the results demonstrate that neck formation is one of the dominant factors controlling the mechanical behavior of sintered microstructures. Increasing d_{ij} enhances the neck ratio, leading to improved load transfer efficiency and reduced stress localization. However, the relatively low coefficient of determination (R^2), particularly for Young's modulus, indicates that neck size alone cannot fully describe the mechanical

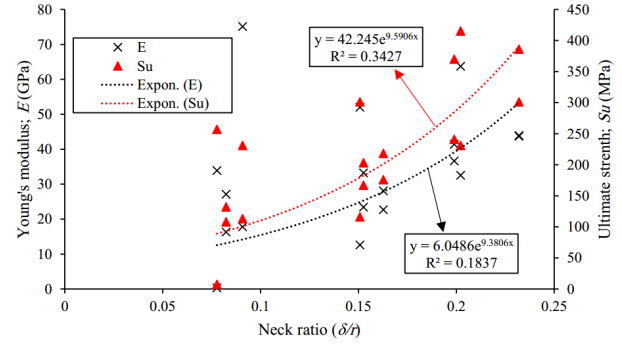

Fig. 8. Dependence of Young's modulus (E) and ultimate strength (Su) on the neck ratio (δ/r) for all generated microstructures. The data points represent individual simulations, while the dashed curves indicate exponential fits. Both stiffness and strength increase nonlinearly with neck ratio, highlighting the fundamental role of inter-particle neck formation in governing load transfer. The relatively higher correlation for strength suggests that failure behavior is more sensitive to neck development than elastic response.

response. The observed scatter highlights the significant influence of additional morphological parameters, such as particle size distribution and connectivity, which interact with neck formation to govern the overall behavior.

3.3.5. Role of particle size distribution (CV)

The effect of particle size distribution on the mechanical response is evaluated using the coefficient of variation (CV), which quantifies the degree of heterogeneity in particle sizes within each microstructure. The generated microstructures exhibit CV values ranging from 0.15 to 0.30, representing different levels of particle size dispersion and microstructural heterogeneity.

The relationship between CV and mechanical properties is further illustrated in Fig. 9, where Young's modulus (E) and ultimate strength (Su) are plotted as a function of CV. In contrast to the overlap parameter, an overall decreasing trend is observed, where both stiffness and strength tend to reduce with increasing CV. This behavior reflects the increasing heterogeneity of the microstructure, which disrupts uniform load transfer and promotes stress concentration and strain localization. To quantify this trend, exponential decay functions were fitted to the data. The Young's modulus can be approximated as Eq. 15.

$$E=363.4\, e^{-11.56\,CV};\ \ (R^2=0.1657) \tag{15}$$

while the ultimate strength follows Eq. 16.

$$Su=1568\, e^{-9.351\,CV};\ \ (R^2=0.1937) \tag{16}$$

These results indicate that both stiffness and strength exhibit a negative exponential dependence on CV. However, the relatively low coefficients of determination (R^2) suggest that particle size variation alone is not sufficient to fully describe the mechanical response. At higher CV values (e.g., case 02 with CV ≈ 0.30), the mechanical response becomes highly unstable, particularly under Y-direction loading, where both stiffness and strength are significantly reduced. This can be attributed to large disparities in particle sizes, which create non-uniform load paths and localized deformation zones. In contrast, microstructures with lower CV values (e.g., case 05 with CV ≈ 0.15) exhibit more stable and balanced mechanical behavior. The reduced

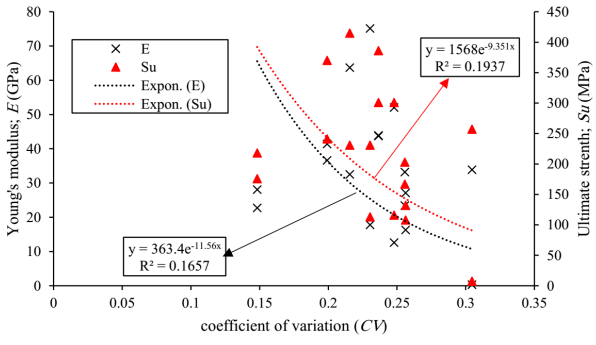

Fig. 9. Variation of Young's modulus (E) and ultimate strength (Su) as a function of the coefficient of variation (CV). The scatter points represent individual simulations, while the dashed lines indicate exponential fits. Both stiffness and strength exhibit a decreasing trend with increasing CV, reflecting the influence of particle size heterogeneity on load transfer and mechanical stability.

size variability leads to a more homogeneous stress distribution and minimizes the formation of critical weak regions. For intermediate CV values, the mechanical response remains scattered, indicating that the effect of particle size distribution is strongly influenced by other morphological parameters. In particular, microstructures with similar CV values may exhibit significantly different mechanical properties due to variations in connectivity and neck formation.

3.3.6. Influence of connectivity (Z_{av})

The influence of particle connectivity on the mechanical response is evaluated using the average degree of connectivity (Z_{av}), which represents the average number of contacts between neighboring particles. This parameter provides a direct measure of the number of available load transfer paths within the microstructure.

The relationship between connectivity and mechanical properties is illustrated in Fig. 10, where Young's modulus (E) and ultimate strength (Su) are plotted as a function of Z_{av}. In general, both stiffness and strength tend to increase with increasing connectivity, indicating that a higher number of inter-particle contacts enhances load distribution and improves mechanical stability. To quantify this trend, exponential functions were fitted to the data. The Young's modulus can be expressed as Eq. 17.

$$E = 1.1035e^{1.3647Z_{av}}, \quad (R^2 = 0.0477) \tag{17}$$

while the ultimate strength follows Eq. 18.

$$Su = 17.278e^{1.0241Z_{av}}, \quad (R^2 = 0.0479) \tag{18}$$

Although both properties exhibit a positive correlation with connectivity, the very low coefficients of determination ($R^2 \approx 0.05$) indicate a weak predictive relationship. This suggests that, unlike overlap or randomness index, connectivity alone is insufficient to accurately describe the mechanical response of the microstructures. The scatter observed in Fig. 10 further highlights this limitation. For instance, microstructures with similar connectivity values ($Z_{av} \approx 2.2$–2.3) exhibit a wide range of stiffness and strength values. This variability indicates that the effectiveness of load transfer paths depends not only on their number but also on their spatial distribution, orientation, and the size of inter-particle necks. At higher connectivity levels (e.g., case 08 with Z_{av} = 2.73), improved mechanical performance is observed, particularly in terms of ultimate strength. This can be attributed to the presence of multiple interconnected load paths, which enable more efficient stress redistribution and delay the onset of localized deformation. However, similar levels of connectivity in other cases do not necessarily result in comparable mechanical behavior, reinforcing the idea that connectivity must be considered in conjunction with other morphological parameters.

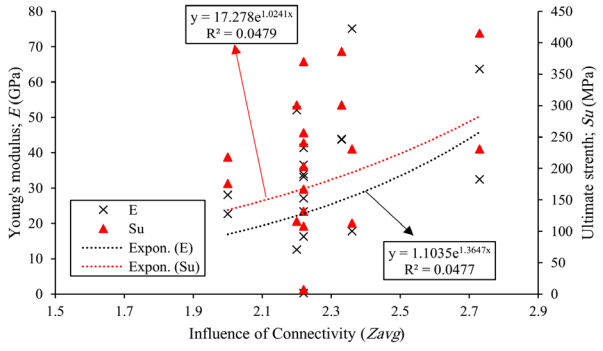

Fig. 10. Dependence of Young's modulus (E) and ultimate strength (Su) on the average degree of connectivity (Z_{av}) for all generated microstructures. The data points represent individual simulations, and the dashed curves indicate exponential fits. Although a general increasing trend is observed, the significant scatter and low correlation highlight the limited predictive capability of connectivity when considered independently.

3.3.7. Randomness index as a unified descriptor

To provide a comprehensive measure of microstructural heterogeneity, the randomness index (RI), defined as a combination of particle size dispersion (CV) and connectivity (Z_{av}), is employed as a unified descriptor of the microstructure. This parameter captures the combined effects of size variability and structural connectivity, which together govern the efficiency of load transfer and deformation behavior.

The RI values vary across the generated microstructures, reflecting different levels of structural disorder. Higher RI values correspond to structures with greater size heterogeneity and/or lower effective connectivity, while lower RI values indicate more uniform and well-connected particle networks.

The relationship between RI and mechanical properties is further illustrated in Fig. 11, where Young's modulus (E) and ultimate strength (Su) are plotted as a function of RI. In contrast to individual parameters such as CV or Z_{av}, a clearer and more consistent decreasing trend is observed, where both stiffness and strength reduce with increasing RI.

To quantify this relationship, power-law functions were fitted to the data. The Young's modulus can be approximated as Eq. 19.

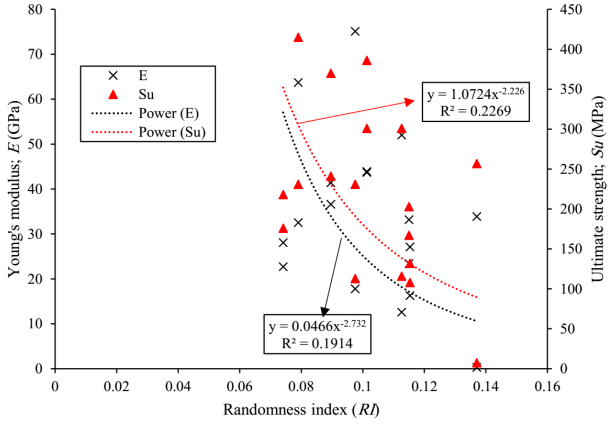

Fig. 11. Dependence of Young's modulus (E) and ultimate strength (Su) on the randomness index (RI) for all generated microstructures. The data points represent individual simulations, and the dashed curves correspond to power-law fits. Both stiffness and strength decrease nonlinearly with increasing RI, indicating the combined effect of particle size dispersion and connectivity on mechanical performance. Compared to individual parameters, RI provides a more consistent correlation with mechanical behavior.

$E=0.0466\,RI^{-2.732}$; ($R^2=0.1914$) (19)

while the ultimate strength follows Eq. 20.

$Su=1.0724\,RI^{-2.226}$; ($R^2=0.2269$) (20)

These results indicate that both stiffness and strength exhibit an inverse nonlinear dependence on RI, highlighting the critical role of combined morphological disorder in governing mechanical performance. Compared to CV and Z_{av} individually, the *RI* provides a more consistent correlation with mechanical behavior, particularly for ultimate strength.

Microstructures with higher RI values (e.g., case 02, RI ≈ 0.14) exhibit significantly reduced stiffness and strength, along with pronounced strain localization. This behavior is attributed to the combined effect of high size dispersion and insufficient effective load transfer paths. In contrast, lower RI values (e.g., case 05, RI ≈ 0.07) correspond to more uniform and well-connected structures, resulting in improved load distribution and enhanced mechanical performance.

Overall, the results demonstrate that the randomness index serves as a robust and unified descriptor for evaluating the mechanical behavior of sintered microstructures. By integrating the effects of particle size distribution and connectivity, RI provides a more reliable predictor of stiffness, strength, and deformation behavior compared to individual morphological parameters.

3.4. Correlation analysis and structure–property relationships

To establish a comprehensive structure–property relationship, the effects of key morphological parameters, including overlap distance (d_{ij}), neck ratio (δ/r), coefficient of variation (CV), average connectivity (Z_{av}), and randomness index (RI), were comparatively analyzed in relation to the mechanical properties.

The results indicate that different parameters play distinct roles in governing mechanical behavior. The overlap distance and neck ratio exhibit a clear and physically meaningful positive correlation with stiffness and strength, confirming that neck formation is the primary mechanism controlling load transfer efficiency. In contrast, CV shows a negative influence, where increased size heterogeneity promotes stress concentration and strain localization. Z_{av} contributes positively by increasing the number of load paths; however, its predictive capability remains limited when considered independently.

Among all parameters, RI provides the most consistent and comprehensive correlation with mechanical behavior. By combining the effects of particle size distribution and connectivity, RI captures the overall degree of structural disorder and its impact on load transfer mechanisms. Compared to individual parameters, RI demonstrates a more stable relationship with both stiffness and strength, making it a more reliable descriptor for predicting mechanical performance.

These findings suggest that the mechanical behavior of sintered microstructures cannot be described by a single parameter alone, but rather by the combined interaction of multiple morphological features. In particular, neck formation governs the fundamental load transfer mechanism, while structural randomness controls the efficiency and uniformity of this process.

4. Conclusions

In this study, the mechanical behavior of sintered titanium microstructures was systematically investigated using meso-scale numerical modeling, with particular emphasis on the role of morphological characteristics. A series of two-dimensional random microstructures with controlled overlap levels (5–15 μm) were analyzed under directional loading conditions.

The results demonstrate that mechanical performance is strongly governed by microstructural morphology, particularly inter-particle neck formation. Increasing the overlap distance from 5 to 15 μm led to a substantial enhancement in stiffness and strength, with Young's modulus increasing from as low as 0.3 GPa to over 60 GPa and ultimate strength reaching up to 415 MPa. This improvement is directly associated with the growth of inter-particle necks, which enhances load transfer efficiency and reduces stress localization.

The effect of particle size distribution, quantified by the coefficient of variation (CV = 0.15–0.30), was found to be significant but not independently predictive. Higher CV values promoted structural heterogeneity, leading to stress concentration and strain localization, whereas lower CV values resulted in more uniform deformation behavior. Similarly, connectivity (Z_{av} = 2.00–2.73) improved load transfer by increasing the number of available load paths; however, its correlation with mechanical properties remained weak when considered alone.

A key contribution of this work is the introduction of the randomness index (RI = 0.07–0.14) as a unified descriptor of microstructural heterogeneity. Compared to individual parameters such as CV and Z_{av}, RI exhibited a more consistent and reliable correlation with both stiffness and strength, effectively capturing the combined influence of size dispersion and connectivity. The results confirm that mechanical performance decreases nonlinearly with increasing RI, highlighting its suitability as a predictive parameter.

Furthermore, the mechanical response was found to be inherently anisotropic, with stiffness ratios (E_y/E_x) varying from 0.01 to 4.22 depending on microstructural topology. This anisotropy arises from the formation of preferential load paths and is governed by both global morphology and local structural features.

Overall, the findings demonstrate that the mechanical behavior of sintered microstructures cannot be described by a single morphological parameter, but rather by the interaction of neck formation, size distribution, and connectivity. The proposed framework, with the randomness index as a key descriptor, provides a robust basis for microstructure-informed design and optimization of sintered materials.

CRediT authorship contribution statement

Ata Khabaz-Aghdam: Conceptualization; Methodology; Project administration; Software; Supervision; Writing – original draft; Writing– review & editing; Data curation; Investigation.
Bahati M. Clément: Software.
Abuzar E'shagi-Oskui: Writing– review & editing; Data curation; Investigation.

Data availability

The data underlying this article will be shared on reasonable request to the corresponding author.

Declaration of competing interest

The authors declare no competing interests.

Funding and acknowledgment

The authors would like to express their sincere appreciation to the Mechanical Engineering Department of Kyrenia University for their valuable support, cooperation, and contributions throughout the course of this study.

References

[1] E. Marin, A. Lanzutti, Biomedical applications of titanium alloys: a comprehensive review, Materials. 17 (2023) 114. https://doi.org/10.3390/ma17010114.

[2] M.K. Yadav, A. Yarlapati, Y.N. Aditya, P. Kesavan, V. Pandey, et al., Processing and development of porous titanium for biomedical applications: a comprehensive review, J. Manuf. Mater. Process. 9 (2025) 401. https://doi.org/10.3390/jmmp9120401.

[3] A.O. Tyou, A. Khabaz-Aghdam, Finite element analysis of additive manufacturing-enabled cellular architectures for morphing airfoil applications, Synth. Sinter. 6 (2026) 41–48. https://doi.org/10.53063/synsint.2026.61323.

[4] R. Bjørk, V. Tikare, H.L. Frandsen, N. Pryds, The effect of particle size distributions on the microstructural evolution during sintering, J. Am. Ceram. Soc. 96 (2013) 103–110. https://doi.org/10.1111/jace.12100.

[5] A. Shugwurov, Microstructure and Mechanical Properties of Titanium Alloys, Metals. 11 (2021) 1617. https://doi.org/10.3390/met11101617.

[6] S. Digole, S. Karki, M. Mugale, A. Choudhari, R.K. Gupta, T. Borkar, Spark plasma sintering of pure titanium: microstructure and mechanical characteristics, Materials. 17 (2024) 3469. https://doi.org/10.3390/ma17143469.

[7] F. Ternero, L.G. Rosa, P. Urban, J.M. Montes, F.G. Cuevas, Influence of the total porosity on the properties of sintered materials—a review, Metals. 11 (2021) 730. https://doi.org/10.3390/met11050730.

[8] N. Chawla, X. Deng, Microstructure and mechanical behavior of porous sintered steels, Mater. Sci. Eng: A. 390 (2005) 98–112. https://doi.org/10.1016/j.msea.2004.08.046.

[9] A. Khabaz-Aghdam, T.H. Nyenyewa, J.K. Kahungwa, C.M. Bükeç, H.D. Özalp, Porosity-dependent mechanical properties of sintered titanium: RVE-based finite element modeling and Gibson–Ashby analysis, Synth. Sinter. 5 (2025) 323–331. https://doi.org/10.53063/synsint.2025.54317.

[10] N. Wu, F. Xue, J. He, K. Luo, F. Luo, Effects of sintering temperature on the microstructure evolution and mechanical properties of TiB_2–20 wt% CoNi cermets, J. Alloys Compd. 988 (2024) 174259. https://doi.org/10.1016/j.jallcom.2024.174259.

[11] C. Torres-Sanchez, F.R. Al Mushref, M. Norrito, K. Yendall, Y. Liu, P.P. Conway, The effect of pore size and porosity on mechanical properties and biological response of porous titanium scaffolds, Mater. Sci. Eng: C. 77 (2017) 219–228. https://doi.org/10.1016/j.msec.2017.03.249.

[12] L. Gao, J. Liu, X. Cheng, S. Li, Y. Luo, Q. Guo, Effects of short time electric pulse heat treatment on microstructures and mechanical properties of hot-rolled Ti–6Al–4V alloy, Mater. Sci. Eng: A. 618 (2014) 104–111. https://doi.org/10.1016/j.msea.2014.08.085.

[13] P. Zacharopoulos, V.L. Tagarielli, Numerical modelling of the mechanical response of cellular solids made from sintered titanium powders, Int. J. Solids Struct. 113 (2017) 241–254. https://doi.org/10.1016/j.ijsolstr.2017.03.004.

[14] K. Chen, H. Qin, Z. Ren, Establishment of the microstructure of porous materials and its relationship with effective mechanical properties, Sci. Rep. 13 (2023) 18064. https://doi.org/10.1038/s41598-023-43439-6.

[15] V. Tikare, M. Braginsky, D. Bouvard, A. Vagnon, Numerical simulation of microstructural evolution during sintering at the mesoscale in a 3D powder compact, Comput. Mater. Sci. 48 (2010) 317–325. https://doi.org/10.1016/j.commatsci.2010.01.013.

[16] U. Khristenko, A. Constantinescu, P. Le Tallec, J.T. Oden, B. Wohlmuth, A statistical framework for generating microstructures of two-phase random materials: application to fatigue analysis, Multiscale Model. Simul. 18 (2020) 21–43. https://doi.org/10.48550/arXiv.1907.02412.

[17] A.P. Roberts, E.J. Garboczi, Elastic properties of model random three-dimensional open-cell solids, J. Mech. Phys. Solids. 50 (2002) 33–55. https://doi.org/10.1016/S0022-5096(01)00056-4.

[18] S. Muñoz, S.M. Castillo, Y. Torres, Different models for simulation of mechanical behaviour of porous materials, J. Mech. Behav. Biomed. Mater. 80 (2018) 88–96. https://doi.org/10.1016/j.jmbbm.2018.01.026.